Inorganic Chemistry

Article

pubs.acs.org/IC

Phase Range of the Type-I Clathrate $Sr_8Al_xSi_{46-x}$ and Crystal Structure of $Sr_8Al_{10}Si_{36}$

John H. Roudebush,[†] Naohito Tsujii,[†,‡] Antonio Hurtando,[†] Håkon Hope,[†] Yuri Grin,[§] and Susan M. Kauzlarich*[,†]

[†]Department of Chemistry, University of California, One Shields Avenue, Davis, California 95616, United States

[‡]National Institute for Materials Science, Tsukuba 305-0047, Japan

[§]Max-Planck-Institut für Chemische Physik Fester Stoffe, 01187 Dresden, Germany

Supporting Information

ABSTRACT: Samples of the type-I clathrate $Sr_8Al_xSi_{46-x}$ have been prepared by direct reaction of the elements. The type-I clathrate structure (cubic space group $Pm\bar{3}n$) which has an Al−Si framework with Sr^{2+} guest atoms forms with a narrow composition range of $9.54(6) \leq x \leq 10.30(8)$. Single crystals with composition $A_8Al_{10}Si_{36}$ (A = Sr, Ba) have been synthesized. Differential scanning calorimetry (DSC) measurements provide evidence for a peritectic reaction and melting point at ~1268 and ~1421 K for $Sr_8Al_{10}Si_{36}$ and $Ba_8Al_{10}Si_{36}$, respectively. Comparison of the structures reveals a strong correlation between the 24*k*-24*k* framework sites distances and the size of the guest cation. Electronic structure calculation and bonding analysis were carried out for the ordered models with the compositions $A_8Al_6Si_{40}$ (6*c* site occupied completely by Al) and $A_8Al_{16}Si_{30}$ (16*i* site occupied completely with Al). Analysis of the distribution of the electron localizability indicator (ELI) confirms that the Si−Si bonds are covalent, the Al−Si bonds are polar covalent, and the guest and the framework bonds are ionic in nature. The $Sr_8Al_6Si_{40}$ phase has a very small band gap that is closed upon additional Al, as observed in $Sr_8Al_{16}Si_{30}$. An explanation for the absence of a semiconducting "$Sr_8Al_{16}Si_{30}$" phase is suggested in light of these findings.

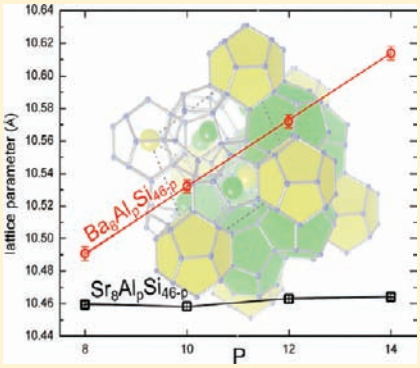

INTRODUCTION

Clathrates are compounds that consist of an open cage-forming framework with an enclosed chemical species. The clathrate structure is of great general interest. The coexistence of different chemical species, those in the framework itself and another in the cage, provides for an unusual degree of variability in properties.[1,2] Clathrates are important in both the natural and the synthetic worlds. For example, clathrate hydrates can be formed from water molecules surrounding methane, acting as a natural gas storage material.[1,3] Intermetallic clathrates are of interest to the thermoelectric community because of their cage structure and the wide range of elements that can be incorporated to adjust their thermoelectric efficiency (ZT).[2]

Figure 1 shows the building blocks for the type-I clathrate structure. The crystallographic space group is $Pm\bar{3}n$. The structure consists of a framework of 4-coordinate atoms that form two polyhedral cages of different sizes. There are three crystallographically distinct sites in the framework, denoted by the Wyckoff symbols 24*k*, 16*i*, and 6*c*. The smaller cage is a dodecahedron of pentagons (Figure 1a). It is made up from the 24*k* and 16*i* framework atoms. The center of the cage is located at the Wyckoff site 2*a*; it is typically occupied by an electropositive element from group 1 or 2. The larger cage, a tetrakaidecahedron of six pentagons and two hexagons (Figure 1b), is made up from the 24*k*, 16*i*, and 6*c* framework sites. The

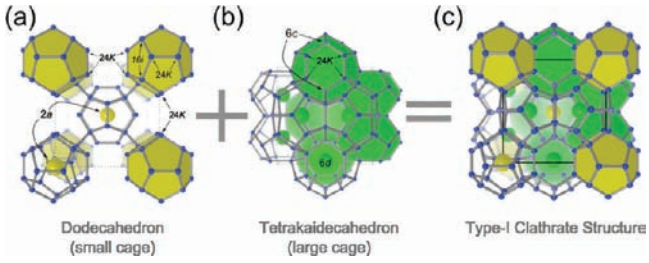

Figure 1. Building units of the type-I clathrate structure. (a) Dodecahedron, (small cage) formed from the 24*k* and 16*i* Wyckoff sites with 2*a* site in the center. (b) Tetrakaidecahedron (large cage) formed from 24*k*, 16*i*, and 6*c* sites. (c) Face-sharing of cages results in the type-I clathrate structure.

center of the cage is at the 6*d* site, also occupied by an element from group 1 or 2. Figure 1c shows the full clathrate structure that is formed from a fusion of the two types of cages. A typical formula would be $(1/2)_8(TM/13)_x(14)_{46-x}$ where (1/2) is a group 1 or 2 element, TM/13 a transition metal or a group 13 element, and (14) a group 14 element. Binary, ternary, and

Received: November 23, 2011
Published: March 20, 2012

   dx.doi.org/10.1021/ic2024814 | *Inorg. Chem.* 2012, 51, 4161−4169

quaternary type-I clathrates can be formed by substitution of various elements on the different sites.[1,4,5]

Germanium-based clathrates have demonstrated high thermoelectric efficiency in $Ba_8Ga_{16}Ge_{30}$,[6,7] glass-like thermal conductivity in $Sr_8Ga_{16}Ge_{30}$,[8] and ferromagnetism in $Eu_8Ga_{16}Ge_{30}$.[9] The thermoelectrically relevant properties of two modifications of $Eu_8Ga_{16}Ge_{30}$ are strongly influenced by chemical composition.[10,11] Si-containing clathrates have been less studied as thermoelectric materials, but they have shown superconductivity in $Ba_{8-x}Si_{46}$[12−14] and $Na_2Ba_6Si_{46}$[15] as well as hydrogen encapsulation in $K_{8-x}(H_2)_ySi_{46}$.[16] Many of the silicon-based clathrates, including the first compounds reported, $Na_{24}Si_{126}$ and Na_8Si_{46}, do not follow Zintl electron counting and exhibit metallic properties.[17,18] Recently, a cationic silicon-based clathrate, $Si_{46-x}P_xTe_y$, has been reported and shows a wide homogeneity range suggesting that Si containing clathrate phases may have complex structure−property relationships.[19] Relative to Ge-based clathrates, thermoelectric materials made from aluminum or silicon would provide an attractive alternative in terms of price, weight, and environmental impact. Some $Ba_8Al_xSi_{46-x}$ phases have been studied,[20−23] but show higher thermal conductivity and lower thermopower values than their Ga−Sn and Ga−Ge counterparts. The poor performance of the Ba−Al−Si systems has been attributed to an inability to optimize their electronic properties.[22,23] In the present study, the phase stability and crystal structure of $Sr_8Al_xSi_{46-x}$ are explored to better understand the host−guest relationship between the enclosed cation and the framework.

It would be desirable to study the thermoelectric properties of $Sr_8Al_{16}Si_{30}$; however, the synthesis of a compound of this composition has proven elusive, for reasons that are not clear. Recently, the structure and thermoelectric properties of the $Ba_7SrAl_{14}Si_{32}$ phase have been reported.[23] In this case the maximum solubility of Sr in the $Ba_8Al_{14}Si_{32}$ compound was found to be only 1.3 atoms/formula unit. However, as Sr^{2+} has a smaller radius than Ba^{2+} it should easily fit into both the large and the small cages of the type-I clathrate structure. Furthermore, $Sr_8Ga_{16}Ge_{30}$ (a = 10.723 Å)[4] has a larger lattice parameter than $Ba_8Al_{15}Si_{31}$ (a = 10.614 Å)[22] and is reported to be stable. Therefore, the absence of the clathrate-I structure at the composition $Sr_8Al_{16}Si_{30}$ is perplexing.

In this study the potential synthesis of clathrates with the composition $Sr_8Al_xSi_{46-x}$ for x = 8, 10, 12, 14 is explored. Crystal structures of $A_8Al_{10}Si_{36}$ (A = Sr, Ba) are reported, the former being the first for a $Sr_8Al_xSi_{46-x}$ type-I clathrate structure. The structures of these phases are compared, in an effort to better understand the interaction between guest cation and framework structure. A detailed comparison of the structures provides insight to why $Sr_8Al_{16}Si_{30}$ has not yet been prepared.

EXPERIMENTAL SECTION

Synthesis. Strontium (Alfa Aesar, 99.99%) or barium (Sigma Aldrich, 99.99%) and aluminum (Sigma-Aldrich, 99.999+%) were used as received and weighed in an argon-filled glovebox with less than 1 ppm of water. Silicon pieces (Aesar, 99.99999%) were weighed under ambient conditions. All samples were arc-melted on a copper-cooled hearth to obtain a button with mass between 1 and 1.5 g and diameter ∼1 cm. To determine the phase range of the Sr−Al−Si type-I clathrate, syntheses with starting atomic ratios 8.2Sr:pAl:46-pSi with p = 8, 10, 12, 14, were performed by arc melting. The excess Sr (2.5% atomic) was provided to compensate for loss due to evaporation. Mass loss after arc-melting was typically between 1 and 2%. Arc-melted ingots were sealed in quartz jackets and annealed at 1073 K for 4 days. Throughout this paper, p indicates the amount used in the synthesis and x indicates the resulting nominal composition of the clathrate phase determined from microprobe analysis.

To study the thermal stability of the p = 10 sample, pieces of the arc-melted ingot of 8.1Sr:10Al:36Si were placed in alumina crucibles and sealed in quartz jackets. These samples were annealed at 1273 K (6 days), 1173 K (6 days), and 1073 K (4 days).

Crystals with composition $Sr_8Al_{10}Si_{36}$ were grown using an arc-melted ingot of 8.1Sr:10Al:35Si in a boron-nitride crucible cut into a conical shape. A piece of the arc-melted ingot was cut and heated in the BN crucible to 1273 K and then slowly cooled to 1173 at 2 K/h. Single crystals were extracted from the sample.

$Ba_8Al_{10}Si_{36}$ samples were prepared by arc-melting the elements with the ratio 8.2Ba:10Al:36Si. Upon cooling, single crystals grew from the melt and were directly extracted from the ingot.

Powder X-ray Diffraction (PXRD). Powder diffraction patterns were collected from 10 to 90° in 2θ on a Bruker D8 Advance diffractometer employing Cu Kα radiation (λ = 1.5418 Å, 40 kV, 40 mA). Rietveld refinement was performed with the program FullProf.[24] Lattice parameters were refined using diffraction peaks up to 77° in 2θ. Weight % of identified phases in the $Sr_8Al_xSi_{46-x}$ samples were determined by Rietveld fits. The data and fits are provided as Supporting Information.

Electrical Transport. The Quantum Design magnetic property measurement system (MPMS) was used as a field and temperature platform interfaced with a Keithley current and voltage source to measure the electrical resistivity of the ingot from which a single crystal of $Sr_8Al_{10}Si_{36}$ was abstracted. A four-probe method was employed to measure electrical resistance (10 mA applied current, temperature from 300 to 2 K). Platinum electrical leads were affixed to the sample with silver paint 1.43 mm apart. The cross sectional area of the ingot was 1.46 mm^2.

Microprobe Analysis. The single crystals that had been used for X-ray diffraction measurements were mounted in epoxy and polished for analysis on a Cameca SX-100 electron microprobe equipped with five wavelength-dispersive spectrometers. The standards $SrAl_2Si_2$, $BaAl_{3.54}Si_{0.41}$, Al and Si were used for Sr, Ba, Al, and Si, respectively. Data were collected from a series of points separated by at least 5 μm; resulting weight percentage totals were within 1% of 100%. Atomic percentages were used to calculate nominal compositions. A table of atomic % and compositions is provided in Supporting Information.

Thermogravimetric Analysis (TGA)/Differential Scanning Calorimetry (DSC). Samples were prepared for thermal analysis by cutting a piece (30−40 mg) from the heat-treated ingot from which the single crystals of $A_8Al_{10}Si_{36}$ (A = Sr, Ba) were obtained. A Netzsch Thermal Analysis STA 409 was employed to measure thermal properties between 300 and 1473 K. Sample pellets were placed in an alumina crucible with lid and heated under flowing Ar at 10 K/min. Data were collected at 4 pts/K. The thermal cycle and measurements were run two consecutive times for the $Ba_8Al_{10}Si_{36}$ sample.

Single-Crystal X-ray Diffraction. A crystal of $Sr_8Al_{10}Si_{36}$ with the dimensions 0.119 × 0.150 × 0.187 mm was cut from a larger crystal ingot and mounted on a glass fiber. A crystal of $Ba_8Al_{10}Si_{36}$ with dimensions 0.121 × 0.127 × 0.165 mm was extracted from the arc-melted pellet. Both samples were measured at 90 K with a Bruker Smart Apex II diffractometer with Mo K_α radiation. An analytical face indexed absorption correction was performed using SADABS.[25]

Initial positional parameters were determined by direct methods (shelxs).[26] Both structures were refined in a similar fashion, in a manner described for $Ba_7Sr_1Al_{14}Si_{32}$.[23] The uncertainties in the refined occupancies were reduced by a factor of 2 if equivalent intensities were not merged. This result was determined to be caused by the presence of systematic errors in the data. The occupancy results for both merged and unmerged data are provided in the Supporting Information. The values are very similar, but the uncertainties are lower in the unmerged data. Therefore, the results presented herein are for the unmerged data. Initially, the total Al content was constrained to that of the microprobe composition, and then mixed Al/Si occupancy was introduced to the 24k, 16i, and 6c framework sites, initially keeping the sites fully occupied. Individual Al and Si occupancies were allowed to vary. Finally, the question of vacancies in the 2a, 6d, and 6c sites was addressed by

dx.doi.org/10.1021/ic2024814 | Inorg. Chem. 2012, 51, 4161−4169

allowing the total occupancies at each site to refine. In the final model, the 6*c* site was restrained to be fully occupied by Al, because the Si occupancy at this site always refined to zero.

Calculation Procedures. Electronic structure calculation and bonding analysis were carried out for the ordered models with the compositions $Sr_8Al_6Si_{40}$, $Ba_8Al_6Si_{40}$ (with the 6*c* site occupied completely by Al) and $Sr_8Al_{16}Si_{30}$, $Ba_8Al_{16}Si_{30}$ (with the 16*i* site occupied completely with Al). The models used the respective lattice parameters and atomic positions from the single crystal X-ray refinement of $Sr_8Al_{10}Si_{36}$ and $Ba_8Al_{10}Si_{36}$ reported in this study (Tables 1 and 2). The TB-LMTO-ASA program package was used.[27]

Table 1. Crystallographic Data and Structure Refinement Parameters for $Sr_8Al_{10}Si_{36}$ and $Ba_8Al_{10}Si_{36}$

temp (K)	90	90
refined composition[a]	$Sr_8Al_{10.32}Si_{35.62}$	$Ba_{7.95}Al_{9.98}Si_{35.95}$
space group:	$Pm\bar{3}n$	
size (mm)	0.119 × 0.150 × 0.187	0.121 × 0.127 × 0.165
a (Å)	10.4495(1)	10.5148(1)
V (Å^3)	1141.00 Å^3	1162.53 Å^3
Z	1	
density (calcd)[a] (Mg/m^3)	2.849	3.395
abs coeff (mm^{-1})	10.41	7.80
θ range	2.76–49.10°	2.74–49.09°
data collection	Bruker Apex II, CCD, λ (Mo K$_\alpha$) = 0.71073 Å	
reflns collected	24632	32664
data/params/restraints	22791/17/1	30266/19/1
$R(\sigma)$	0.0376	0.0321
final *R* indices [$I > 2\sigma(I)$]	R_1 = 0.0278, wR_2 = 0.0522	R_1 = 0.0234, wR_2 = 0.0484
largest diff. peak and hole (fm Å^{-3})	0.51, −0.34	0.50, −0.94

[a]Total Al content determined from microprobe analysis.

The Barth-Hedin exchange potential[28] was employed for the LDA calculations. The radial scalar-relativistic Dirac equation was solved to obtain the partial waves. Because the calculation within the atomic sphere approximation (ASA) includes corrections for the neglect of interstitial regions and partial waves of higher order,[29] an addition of empty spheres was not necessary. The following radii of the atomic spheres were applied for the calculations: *r*(Sr1) = 2.480 Å, *r*(Sr2) = 2.692 Å, *r*(Al1) = 1.491 Å, *r*(Si2) = 1.374 Å, *r*(Si3) = 1.382 Å for $Sr_8Al_6Si_{40}$; *r*(Sr1) = 2.480 Å, *r*(Sr2) = 2.692 Å, *r*(Si1) = 1.491 Å, *r*(Al2) = 1.374 Å, *r*(Si3) = 1.382 Å for $Sr_8Al_6Si_{40}$; *r*(Ba1) = 2.512 Å, *r*(Ba2) = 2.700 Å, *r*(Al1) = 1.477 Å, *r*(Si2) = 1.372 Å, *r*(Si3) = 1.408 Å for $Ba_8Al_6Si_{40}$, and *r*(Ba1) = 2.512 Å, *r*(Ba2) = 2.700 Å, *r*(Si1) = 1.477 Å, *r*(Si2) = 1.372 Å, *r*(Si3) = 1.408 Å for $Ba_8Al_{16}Si_{30}$. For each calculation a basis set containing Ba(6s,5d,4f), Sr(5s,4d), Si(3s,3p), and Al(3s,3p) orbitals was employed for a self-consistent calculation with Ba(6p), Sr(5p,4f), Si(3d) and Al(3d) functions being down-folded. A spin-polarized calculation was performed. The electron localizability indicator (ELI, γ) was evaluated in the ELI-D representation according to refs 30–32 with an ELI-D module within the program package TB-LMTO-ASA.[27] Topological analysis of the electron density, that is, estimation of the shapes, volumes, and charges of the atoms after Bader (QTAIM atoms[33]), and of the electron localizability indicator, for example, localization of the ELI maxima as fingerprints of the direct covalent atomic interactions, was performed with the program Basin.[34]

RESULTS AND DISCUSSION

Phase Relation of the $Sr_8Al_xSi_{46-x}$ and the Type-I Structure. The possible phases in the system $Sr_8Al_xSi_{46-x}$ were investigated by arc-melting and annealing (1073 K) the corresponding mixture of elements. The products typically contained a mixture of phases,[35] including the type-I clathrate, as well as $SrAl_2Si_2$,[36] Si, and $SrSi_2$. Figure 2a provides the estimated weight % of each sample as a function of initial Al

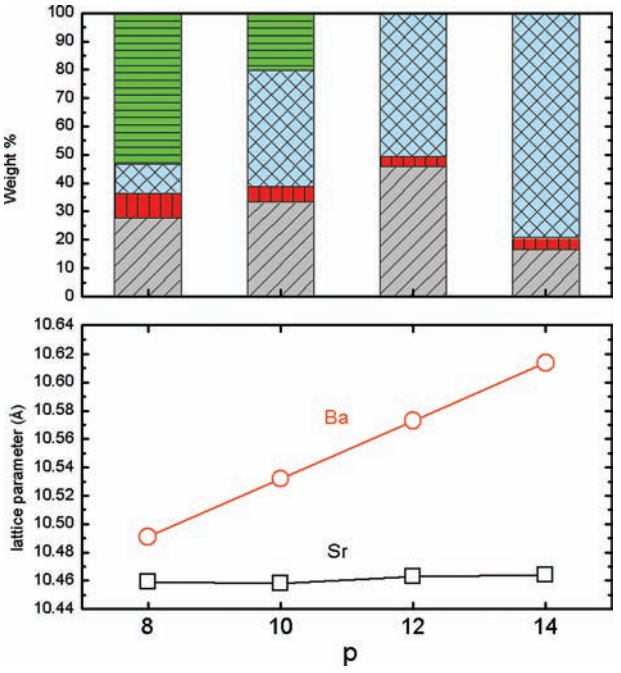

Figure 2. (top) Plot of weight % (indicated by the color and shading of the bar) vs *p* for 8.2A:*p*Al:46-*p*Si, A = Sr, Ba annealed at 1073 K. Weight % key: gray diagonal, clathrate structure; red vertical, Silicon; blue cross, $SrAl_2Si_2$; green horizontal, $SrSi_2$. (bottom) Plot of lattice parameter (Å) of the clathrate phase produced from the starting composition 8.2A:*p*Al:46-*p*Si (A = Sr (squares) and Ba (circles)) as a function of starting aluminum content, *p*. (color online).

Table 2. Refined Site Occupancies, Atoms per Unit Cell, Equivalent Isotropic Displacement Parameters, and Atomic Positions at 90 K

		site occupancy[a]		U_{eq} (Å^2)[b]	
atom, site		$Sr_8Al_{10}Si_{36}$	$Ba_8Al_{10}Si_{36}$	$Sr_8Al_{10}Si_{36}$	$Ba_8Al_{10}Si_{36}$
cation, 2*a*	Sr/Ba	1	0.9866(7)	0.00625(1)	0.00420(1)
cation, 6*d*	Sr/Ba	1	0.9982(6)	0.01352(1)	0.00875(1)
framework, 24*k*	Al	0.036(5)	0.059(5)	0.00789(2)	0.00583(2)
	Si	0.964(5)	0.941(5)	0.00789(2)	0.00583(2)
framework, 16*i*	Al	0.220(7)	0.176(8)	0.00732(3)	0.00570(3)
	Si	0.780(7)	0.836(8)	0.00732(3)	0.00570(3)
framework, 6*c*	Al	0.990(1)	0.989(2)	0.00637(5)	0.00487(5)

[a]Al content was restrained to the microprobe composition. [b]U_{eq} is defined as one-third of the trace of the orthogonalized U^{ij} tensor.

dx.doi.org/10.1021/ic2024814 | Inorg. Chem. 2012, 51, 4161–4169

composition, p (p is the experimental amount of Al in the synthesis). All four samples contain a mixture of phases, indicating that there is no phase-pure composition in the 8Sr:pAl:46-pSi series under these reaction conditions. The p = 8, 10 samples contain 4 phases and therefore have yet to reach equilibrium.

It was expected that the lattice parameter of the clathrate phase would increase with increasing aluminum incorporation, similar to that observed for $Ba_8Al_xSi_{46-x}$ where it was shown that 8.2Ba:pAl:46-pSi resulted in $p = x$, where x corresponds to the amount of Al in the clathrate structure.[22] In the case of $Ba_8Al_xSi_{46-x}$ the increase in lattice parameter (a) can be described as a function of Al content in the synthesis mixture, obeying the equation $a = 10.327(4) + 0.02046(30)x$. Figure 2b shows plots of the lattice parameters for the indexed type-I clathrate structure ingots with the initial ratio of elements: 8.2A:pAl:46-pSi, A = Ba, Sr. It is evident that the clathrate structure corresponding to the formula $Sr_8Al_xSi_{46-x}$ has a small range of lattice parameters (10.4606(11) to 10.4661(9) Å), while the clathrate phase corresponding to $Ba_8Al_xSi_{46-x}$ displays a clear dependence of lattice parameter on increasing Al content (10.491(2) to 10.614(4) Å). The small range in lattice parameter for the clathrate phase identified as $Sr_8Al_xSi_{46-x}$ is consistent with a narrow range of aluminum incorporation. The Al content is confirmed by microprobe analysis where the nominal composition for which the clathrate structure is observed is $x \sim 10$ (see below).

Microprobe analysis was performed on the 8.2Sr:pAl:46-pSi arc-melted and annealed samples, and the composition of the clathrate phase was determined. A fully occupied cation model fits the data best. A narrow composition range of $9.54(6) < x < 10.30(8)$ was found for the homogeneity range of the type-I clathrate $Sr_8Al_xSi_{46-x}$. The fully occupied cation model gives Al + Si sums slightly less than 46 atoms/unit cell, suggesting the presence of a small number of vacancies (~0.5) in the framework. Vacancies could not be confirmed with either Rietveld or single-crystal refinement. This is not surprising, considering the relatively small number of vacancies and the additional complications of distinguishing relative amounts of Al and Si by X-ray diffraction when they occupy the same crystallographic site.[23] The presence of framework vacancies is rare in silicon-based clathrates[37] but is common in germanium clathrates, where vacancies can be rationalized by way of electron counting.[38,39]

A compound of composition $Sr_8Al_{16}Si_{30}$, synthesized directly from the elements, has been previously reported (space group: $Pm\bar{3}n$), with a lattice parameter of 10.47 Å.[4] This lattice parameter value is within the range (with uncertainty) found for the $Sr_8Al_xSi_{46-x}$ series with $x \sim 10$ presented herein. The presence of $SrAl_2Si_2$ as an impurity in the powder X-ray diffraction pattern was also noted; however, the crystal structure or compositional analysis were not reported. It is likely that the composition of this phase is not $Sr_8Al_{16}Si_{30}$ but rather $Sr_8Al_{10}Si_{36}$. On the basis of the data provided above, the nominal composition of the Sr clathrate phase is $Sr_8Al_{10}Si_{36}$ whereas the Ba phase is best described by $Ba_8Al_xSi_{46-x}$.

Growth and Composition of $A_8Al_{10}Si_{36}$ (A = Sr, Ba) Single Crystals. To promote the crystal growth with the x = 10 composition, an arc-melted ingot composition of 8.1Sr:10Al:36Si was annealed at several temperatures. Figure 3 gives the diffraction patterns for the ingot "as cast" and annealed at various temperatures. In the "as cast" sample, $SrAl_2Si_2$ and Si can be identified by their diffraction peaks and in the microprobe analysis

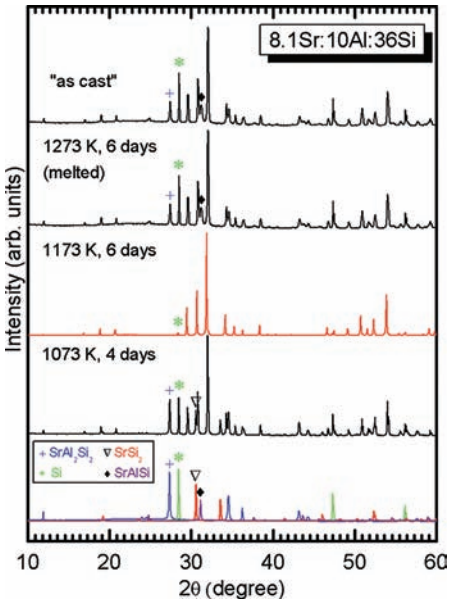

Figure 3. Powder X-ray diffraction of the sample with the starting composition $Sr_{8.1}Al_{10}Si_{36}$, as cast and after annealing at 1073, 1173, 1273 K. The calculated patterns of $SrAl_2Si_2$ (+), Si (*), $SrSi_2$ (∇), and SrAlSi (♦) are given for reference at the bottom (color online).

(Supporting Information). When the arc-melted ingot was heated at 1273 K, it melted. A powder diffraction pattern of the material had obvious peaks corresponding to $SrAl_2Si_2$ and Si. Annealing at 1173 K improves the sample purity, with only a small peak corresponding to Si identified in the powder diffraction pattern. Annealing at slightly lower temperature, 1073 K also promotes the growth of the clathrate phase, but peaks indexed to $SrAl_2Si_2$, Si and $SrSi_2$ can be observed in the powder diffraction pattern. Although the sample annealed at 1173 K appears to be composed primarily of the type-I clathrate phase, single crystals could not be extracted from this sample.

Crystals were grown from a mixture slightly deficient in Si: 8.1Sr:10Al:35Si. The reason for this was that free Si was present in the powder diffraction patterns of the mixture, as indicated in Figure 3, and that Al + Si sums of less than 46 atoms were found in the microprobe analysis. An arc melted ingot with starting composition 8.1Sr:10Al:35Si was heated in a BN crucible and slowly cooled from 1173 to 1073 K; the powder diffraction pattern of this sample indicated the presence of the clathrate phase, $SrAl_2Si_2$, SrAlSi, and Si. Although not phase pure, single crystals of the clathrate phase could be extracted from this ingot. A BSEI of the ingot before and after heating in the BN crucible indicates the homogeneity of the sample is greatly improved after the heat treatment (Supporting Information).

Unlike the $Sr_8Al_xSi_{46-x}$ clathrate system, the $Ba_8Al_xSi_{46-x}$ system has a wider compositional range, and single crystals can be readily formed from the melt. Recently, results on the $Ba_8Al_xSi_{46-x}$ series demonstrated that for the range $8 \leq x \leq 15$ the type-I clathrate phase is the majority phase.[22] The x = 10 composition was chosen for study because it represents an appropriate comparison to the crystal structure of $Sr_8Al_{10}Si_{36}$.

The composition for the single crystals, $A_8Al_{10}Si_{36}$ (A = Sr, Ba), calculated from microprobe data is provided in Table 1. The crystals used in the microprobe analysis are also the ones used for single crystal X-ray diffraction and BSEI. Elemental mapping of the crystals is shown in Figure 4. The Sr crystal is a

dx.doi.org/10.1021/ic2024814 | Inorg. Chem. 2012, 51, 4161–4169

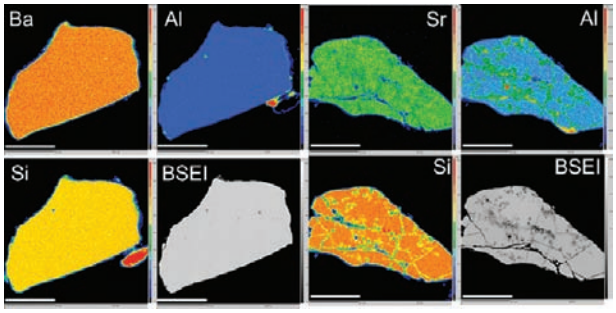

Figure 4. BSEI of the single crystal of $Sr_8Al_{10}Si_{36}$ (left 4 frames) and $Ba_8Al_{10}Si_{36}$ (right 4 frames) used for single crystal X-ray diffraction with the corresponding elemental mapping. The $Sr_8Al_{10}Si_{36}$ crystal is a mosaic. The scale bar shown in the left corner for each image is 50 μm.

mosaic with Al and Si rich phases at the grain boundaries. Both fully occupied cation and fully occupied framework models were applied to calculate nominal clathrate compositions. The fully occupied cation model gave the composition $Sr_{8.0}Al_{10.32(2)}Si_{34.83(4)}$, while the fully occupied framework model gave a composition of $Sr_{8.15(4)}Al_{10.51(2)}Si_{35.49(3)}$. The models suggest there are either 0.86(6) vacancies in the framework or that there are more than 8 Sr atoms per unit cell. The latter is not possible in the type-I clathrate structure, and the additional Sr may be due to contributions from the phases at the grain boundaries (Figure 4). Not surprisingly, single-crystal diffraction, which only measures the diffraction intensities from the clathrate phase, could not confirm the presence of vacancies (see below). Samples from the $Sr_8Al_xSi_{46-x}$ series of annealed ingots also showed preference for the filled-cation model. Therefore the filled cation model was chosen to describe the composition of the single crystal. In contrast to the $Sr_8Al_{10}Si_{36}$ microprobe analysis, the filled-framework model gave the most reasonable nominal composition for the $Ba_8Al_{10}Si_{36}$ crystal.

Electrical resistivity measurements were performed on the 8.1Sr:10Al:35Si ingot composition, of which single crystals could be extracted. The resistivity of the sample in temperature range 2 K–300 K shows metallic behavior (Supporting Information) indicating that if framework vacancies are present, they are not at a quantity sufficient to provide a semiconducting state. This is unlike the $Ba_8Ga_{10}Si_{36}$ system where semiconducting behavior has been reported and attributed to the presence of framework vacancies.[40]

Thermal Analysis. Figure 5 gives the thermal analysis by TG/DSC, performed up to 1473 K of the ingots from which the single crystals were obtained. The $Sr_8Al_{10}Si_{36}$ sample shows a large broad endotherm upon heating, with an onset at 1268 K. This endotherm is assigned to the incongruent melting of the clathrate phase. A smaller endotherm is observed at 1379 K, which is above the melting points of both the $SrAl_2Si_2$ and $SrSi_2$ phases. This may be attributed to the solidus. There are one small and two large exotherms during cooling, with onsets of 1383, 1254, and 1202 K. These are assigned to liquidus, clathrate formation, and ternary eutectic, respectively. $SrAl_2Si_2$ has been reported to crystallize at ~1243 K.[36] The DSC trace for the $Ba_8Al_{10}Si_{36}$ sample shows one endotherm (1421 K) and exotherm (1373 K), characteristic of a congruently melting phase. Once the sample cooled to 825 K, the sample was reheated to 1473 K to check for additional peaks. The second scan was identical to the first, so it is omitted for clarity, but it supports the observation that $Ba_8Al_{10}Si_{36}$ melts congruently.

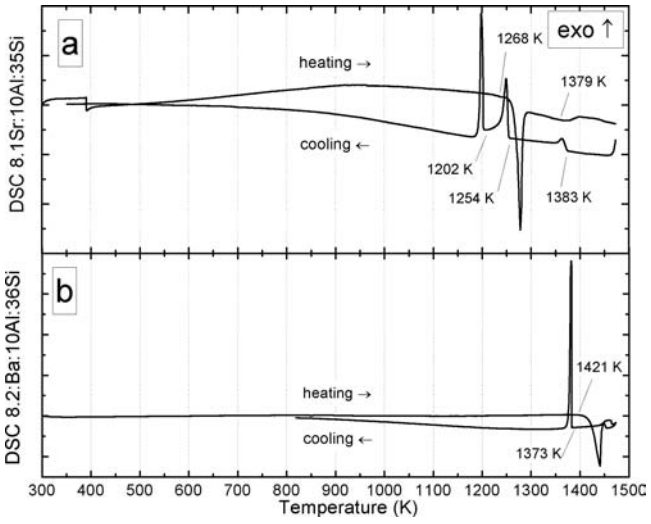

Figure 5. DSC traces for $Sr_8Al_{10}Si_{36}$ (a) and $Ba_8Al_{10}Si_{36}$ (b) samples. Exo- and endotherms are identified by their onsets. Heating rate is 10 K/min.

$A_8Al_{10}Si_{36}$ (A = Sr, Ba) Crystal Structures. Single-crystal data collection and refinement parameters are provided in Table 1. As expected, the Sr-containing phase has a smaller unit cell than the corresponding Ba phase. The lattice parameters are 10.4495 (1) and 10.5148 (1) Å, respectively. However, the framework compositions of the two crystals also differ by 0.34 Al atoms, and the difference in Al content may contribute to the lattice parameter difference.

The lattice parameter in the $Ba_8Al_xSi_{46-x}$ series was found to increase by ~0.02 Å/Al as Al replaced Si. If a similar effect were to occur for $Sr_8Al_{10}Si_{36}$ (taking into account the small difference in Al content), it would result in a lattice parameter about 0.0068 Å longer (0.34 × 0.02 Å) than that observed. However, the observed lattice parameter of the Sr crystal is 0.0653 Å smaller than that of the Ba crystal. The differences in the lattice parameters for the two compounds must therefore be attributed to the size of the cation rather than to the framework composition. The observed lattice parameters can be predicted by taking the lattice parameters for the hypothetical Sr_8Si_{46} phase (~10.257 Å),[41] known Ba_8Si_{46} phase (10.318 Å)[41] and accounting for the 10 Al atom in the framework (adds ~0.2 Å).

Table 2 gives site occupancies and thermal parameters (U_{eq}) from single-crystal refinements. Similar to the microprobe analysis, the Sr occupancies are fully occupied and the Ba occupancies were less than fully occupied. The outcome of the refinement are consistent with trends found in the microprobe measurements. There are three atomic sites in the framework (Wyckoff sites 24*k*, 16*i*, and 6*c*), shown in Figure 6. Atoms in the first two positions, 24*k* and 16*i*, belong to both the large and the small cages, whereas the atoms in the 6*c* site only belong to the larger cage. In both structures, the 6*c* site was found to be only occupied by Al. Both structures prefer Si on the 24*k* site (96 and 94% occupancy for the Sr and Ba compounds, respectively) with mixed occupancy, Al and Si, on the 16*i* site. This is different than what is observed in the $Ba_7Sr_1Al_{14}Si_{32}$[23] structure and other type-I clathrates with larger group 13 incorporations.[42]

In cases with mixed occupancy of sites, as observed in these structures, the two framework atoms may not occupy exactly the same positions.[23,43] In cases where the difference in covalent radius is large, this can be modeled with a split site

dx.doi.org/10.1021/ic2024814 | Inorg. Chem. 2012, 51, 4161–4169

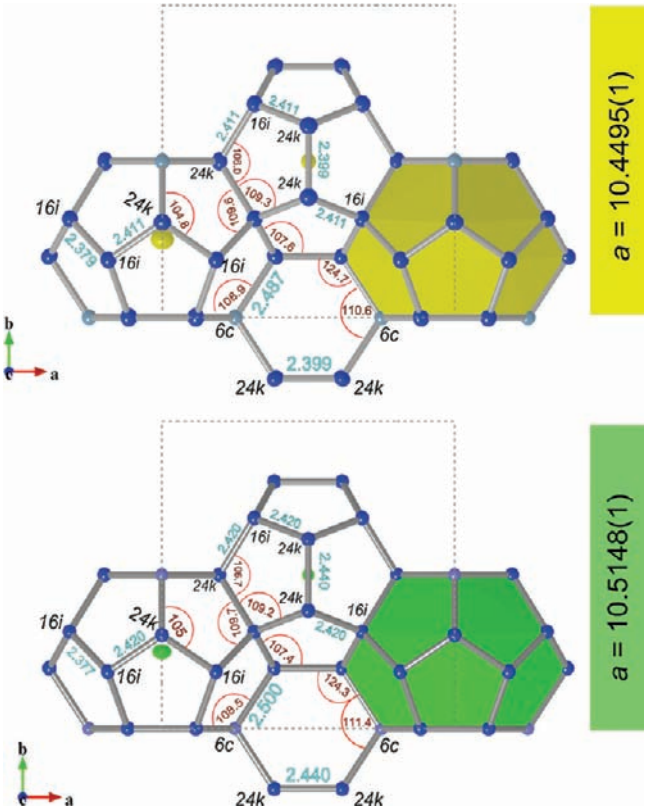

Figure 6. Bond lengths (Å, blue numbers) and angles (deg, red arcs) determined by single-crystal analysis. $Sr_8Al_{10}Si_{36}$ top (yellow coloring) and $Ba_8Al_{10}Si_{36}$ bottom (green coloring). View along the 100 plane. The lattice parameter for each structure is given in Å to its right. Framework atoms are depicted as light and dark blue spheres, Sr as yellow and Ba as green ellipsoids. Wyckoff symbols for selected framework sites are given in black.

position;[43] in more subtle cases, this can be modeled with anisotropic displacement.[44] In both $A_8Al_{10}Si_{36}$ structures, both the 16*i* and 24*k* sites were found to contain mixed occupancy in the final refinement model. Anisotropic displacement is indicated at the 24*k* site, but not at the 16*i* (Supporting Information). This indicates that the Si and Al atoms occupy different positions for the 24*k* site whereas they are much less separated in the 16*i* site.

The distances between Wyckoff sites are presented in Figure 6 and Table 3. Because the type-I clathrate structure has a rigid covalent framework, there should be little tolerance for deformation of framework angles with elemental substitution. Indeed, this is the case. Comparing $Sr_8Al_{10}Si_{36}$ to $Ba_8Al_{10}Si_{36}$, there is only a small difference in bond angles, the largest being 0.8° (24*k*-6*c*-24*k*); therefore the bond distances can be considered for an explanation in the difference of lattice parameters between the two crystals. There are four bonds in the framework: 24*k*-24*k*, 24*k*-6*c*, 24*k*-16*i*, and 16*i*-16*i*. Their lengths are given in Table 3 and Figure 6.

The largest difference in framework bond distances is observed for the 24*k*-24*k* bond distance which is longer by 0.046 Å in the Ba structure. This distance also influences the volume of the small cage. The large cage has two unique distances, 24*k*-6*c* (larger for the Ba structure by 0.0125 Å) and 16*i*-16*i* (smaller in the Ba structure by 0.0015 Å). The 24*k*-16*i* distance is present in both cages and is larger for the Ba structure by 0.0094 Å.

These differences in bond distance are consistent with the refined site occupancies. Specifically, the 24*k* site contains more Al in the Ba structure and therefore the apparent 24*k*-24*k* bond should be longer. Alternatively, since the Ba cation is larger than the Sr cation, the distance for the 24*k*-24*k* needs to be longer and therefore the Ba phase can accommodate more Al on this framework position. Because the 24*k*-24*k* distance is parallel to the [100] direction, it is reasonable to assume it directly influences the lattice parameter.

Table 3 also gives examples of type-I clathrate compounds with similar framework compositions but different cations. The Ba-containing phases show longer distances associated with the 24*k* site compared with the Sr phases. This suggests that regardless of the framework composition, the framework bond lengths adjust to the size of the guest cation. This trend is not limited to ternary clathrates; it is also observed for $(Ba_{1-x}Sr_x)_8Si_{46}$ clathrates.[41]

The observation that the clathrate type-I structure for $Sr_8Al_xSi_{46-x}$ has such a limited composition range suggests that at values other then $x = 10$, the framework distorts to adjust to the smaller cation in such a way as to make the clathrate less stable than competing phases. Replacement of Si with Al in the framework will increase the average bond length, so for $Sr_8Al_xSi_{46-x}$ $x > 10$, additional Al substitution at the 24*k* site is not expected to be favorable because the an increase in the 24*k*-24*k* distance would increase the size of the small cage which could lead to it becoming too large to sustain the framework-guest ionic interaction. Substitution at the 16*i* site with additional Al is also expected to be unfavorable because it will result in Al−Al framework bonds that are expected to be less stable than Al−Si or Si−Si bonds.[44,46] These two effects can explain why the $Sr_8Ga_{16}Ge_{30}$ structure is stable whereas $Sr_8Al_{16}Si_{30}$ is not. In the case of the former, the average bond distances of the framework are longer because of the longer Ga−Ge bonds, and encapsulation of the Sr cation can occur

Table 3. Selected Distances between Framework Atoms (Å) and Lattice Parameters for a Selection of Clathrate Type-I Compounds

Wyckoff symbols	$Sr_8Al_{10}Si_{36}$	$Ba_8Al_{10}Si_{36}$	$Ba_7Sr_1Al_{14}Si_{32}$ [a]	$Ba_8Al_{14}Si_{32}$ [b]	$Sr_8Ga_{16}Ge_{30}$ [c]	$Ba_8Ga_{16}Ge_{30}$ [d]
16*i*-16*i*	2.3786(2)	2.3771(2)	2.3906(7)	2.3885(5)	2.4428	2.446
24*k*-24*k*	2.3933(2)	2.4397(2)	2.4938(6)	2.5030(4)	2.507	2.548
24*k*-16*i*	2.4110	2.4204	2.4468(3)	2.4511(3)	2.4924	2.502
24*k*-6*c*	2.4871	2.4996	2.4975(4)	2.4975(3)	2.4974	2.508
average	*2.425*	*2.439*	*2.461*	*2.465*	*2.491*	*2.505*
lattice parameter	10.4495	10.5148	10.6059	10.6199	10.7236	10.7840

[a] 90 K single crystal data from ref 23. [b] 90 K single crystal data, unpublished results. [c] Neutron powder diffraction 295 K.[8] [d] X-ray powder diffraction 295 K.[45]

dx.doi.org/10.1021/ic2024814 | *Inorg. Chem.* 2012, 51, 4161−4169

with limited contraction of the framework. For the latter phase, the Al−Si bonds are able to contract more with Sr encapsulation, causing the expected clathrate structure to be less stable than that of competing phases. Similarly, both in situ studies at high pressures[47] and density functional theory[48] have shown that the type I clathrate with all Si in the framework, Sr_8Si_{46}, is less stable than its associated binary phases.

To shed more light on the atomic interactions, quantum chemical calculations and analysis of chemical bonding was performed. The ordered model of $Sr_8Al_xSi_{46-x}$ ($Ba_8Al_xSi_{46-x}$) most close to the experimentally found composition with x = 10 is $Sr_8Al_6Si_{46}$ ($Ba_8Al_6Si_{46}$) with 6*c* position occupied by Al and 16*i* and 24*k* sites filled with Si. The electronic density of states reveals a distribution expected from the Zintl counting $[Sr^{2+}]_8[Al^{1-}]_6[Si^0]_{40}\cdot 10e^-$, namely, a small gap below the Fermi level with antibonding states partially occupied (Figure 7, top). The whole DOS is formed mainly by s and p states of Si and partially by the s and p states of Al. These states contribute to all energy ranges proportional to the multiplicity of the crystallographic site. The s and d states of Sr are present in a wide range of energies below the Fermi level and overlap with the s and p states of Si as well as s and p states of Al. This is in agreement with the picture of an ionic guest−host interaction in intermetallic clathrates. A very similar electronic DOS is obtained for the model $Ba_8Al_6Si_{40}$ (Figure 7, middle). The main difference is in the size of the gap below the Fermi level. In case of $Ba_8Al_6Si_{40}$ it is twice as large as for $Sr_8Al_6Si_{46}$.

The model system $Sr_8Al_{16}Si_{30}$ was considered to understand changes in the electronic DOS caused by occupation of the 16*i* site with Al (Figure 7, bottom). Al located at this position shifts the Fermi level to lower energies (as would be expected assuming a rigid band behavior), and contributes to the DOS below the Fermi level. The presence of Al on the 16*i* site leads to closing of the very narrow gap obtained for the $Sr_8Al_6Si_{40}$ model. Because of the smaller size of the gap in the Sr system, it can be closed by a smaller amount of Al when compared with the Ba system. This interpretation of the structure is consistent with the transport measurements (300−4 K) indicating metallic conductivity for $Sr_8Al_{10}Si_{36}$ (Supporting Information).

The interaction between the framework and the guest atoms in intermetallic clathrates is mainly understood as an ionic one. The guest atoms deliver their valence electrons to fulfill the electronic requirements of the framework atoms and the formation of covalent bonds within the framework. Because of the large electronegativity difference between aluminum and silicon, their participation in the same framework is at first glance not obvious. To better understand the role of different elements in the structure, the atomic charges after Bader[33] were calculated. The shapes of the QTAIM atoms (atomic basins) in $Sr_8Al_6Si_{40}$ are shown in Figure 8, top. The atomic basins of Sr have shapes close to spherical, as expected assuming their role as cations (cf. below); the basins of Al and Si resemble the tetrahedral coordination of these atoms and have shapes of the truncated tetrahedra. Integration of the electron density within these basins yields the corresponding charges (Table 4).

Following these charges, alkaline earth metals are the most electropositive and play the role of the cations. Al has also a positive QTAIM charge. Thus the Si−Al bonding should be a polar one. Si atoms differ in the QTAIM charge depending on the site. Because the Si3 atom is in contact with Al, it has a reduced QTAIM charge as compared with Si2, which only has silicon atoms in the first coordination shell.

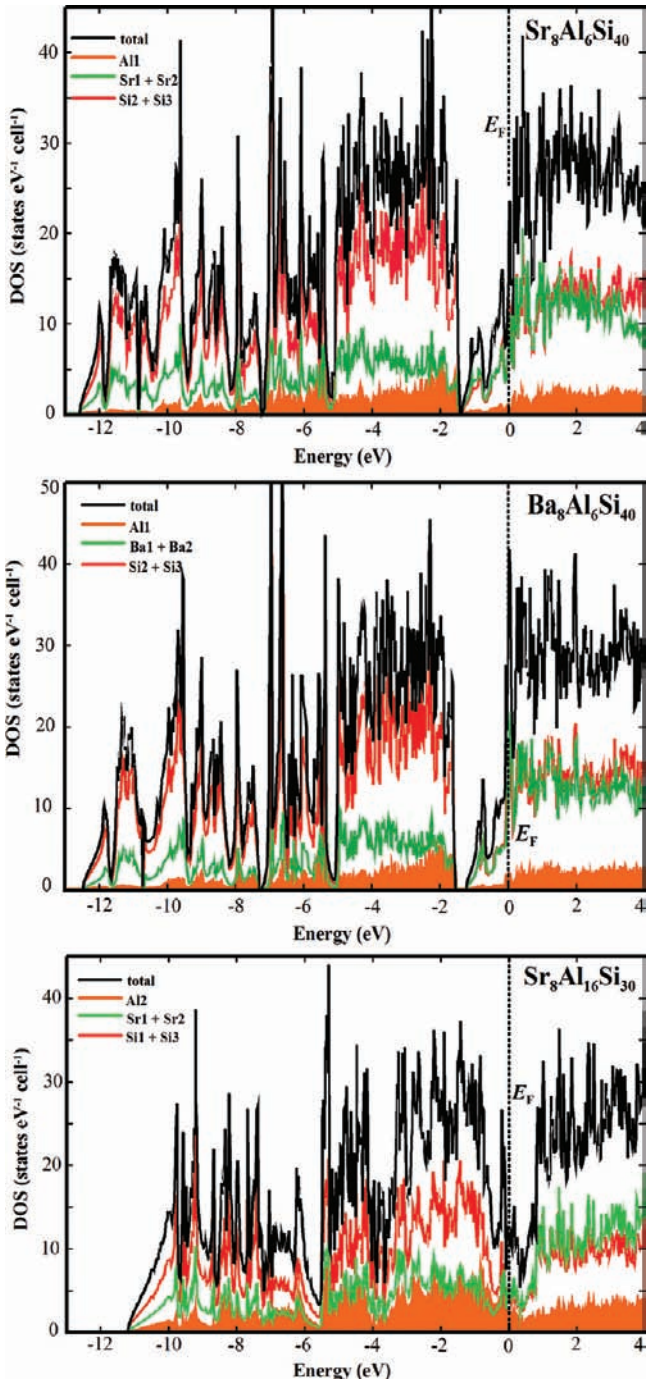

Figure 7. Total electronic density of states together with the contributions of different atoms for the model systems $Sr_8Al_6Si_{40}$, $Ba_8Al_6Si_{40}$, $Sr_8Al_{16}Si_{30}$.

Analysis of the distribution of the electron localizability indicator reveals maxima of ELI between the Al and Si and between Si atoms (Figure 8, bottom) and confirms the direct covalent bonding within the framework. The ELI distribution in the penultimate shells of both Sr species is very close to a spherical one. The structuring in these shells, which can indicate a participation of electrons in these shells bonding in the valence region,[49] is minimal and is weaker than that of Ba in $Ba_8Al_6Si_{40}$ and much weaker than recently observed in $Ba_8Au_6Ge_{40}$.[50] No ELI maxima were found between the Sr atom and the framework atoms, in contrast to that recently

dx.doi.org/10.1021/ic2024814 | Inorg. Chem. 2012, 51, 4161−4169

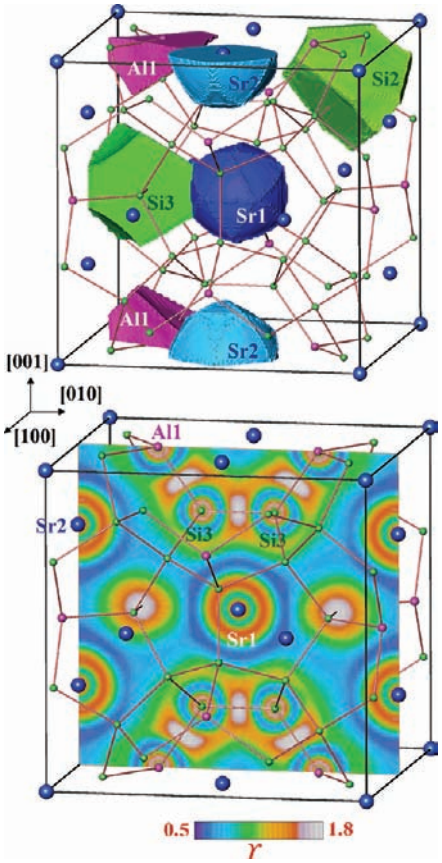

Figure 8. Atomic interactions in $Sr_8Al_6Si_{40}$: (top) The shapes of the QTAIM atoms (atomic basins), the according charges are present in Table 5. (bottom) Distribution of the electron localizability indicator in the plane at $x = 0.5$.

Table 4. QTAIM Charges in $Sr_8Al_6Si_{40}$ and $Ba_8Al_6Si_{40}$

composition	$Sr_8Al_6Si_{40}$	$Ba_8Al_6Si_{40}$
Sr1 (Ba1), 2*a* site	+1.54	+1.30
Sr2 (Ba2), 6*d* site	+1.51	+1.32
Al1, 6*c* site	+1.22	+1.19
Si2, 16*i* site	−0.83	−0.76
Si3, 24*k* site	−0.26	−0.23

found between Ba and Au in $Ba_8Au_6Ge_{40}$. Thus the atomic interactions in $Sr_8Al_6Si_{40}$ and $Ba_8Al_6Si_{40}$ can be summarized as follows: the framework is formed by covalent Si−Si and polar covalent Al−Si bonds; coulomb interactions were found between the cations and the framework.

CONCLUSION

The narrow homogeneity range of the clathrate phase $Sr_8Al_xSi_{46-x}$ around $x \approx 10$, far from the Zintl ideal, has been established by powder diffraction and microprobe analysis. $Sr_8Al_{10}Si_{36}$ melts incongruently at 1254 K, while $Ba_8Al_{10}Si_{36}$ melts congruently at 1421 K. The small phase range observed and absence of vacancies suggests that the stability of $Sr_8Al_xSi_{46-x}$ is governed by factors other reaching a Zintl balance. To further explore reasons for this, the crystal structure of $Sr_8Al_{10}Si_{36}$ is examined and compared to that of $Ba_8Al_{10}Si_{36}$. Comparison of the structures reveals a correlation between framework bond lengths and cation size. In particular, the 24*k*-24*k* distance is the most affected by the size of the cation. A comparison of type-I clathrate structures reveals that this trend is also observed for the $A_8Al_{14}Si_{32}$ and $A_8Ga_{16}Ge_{30}$ frameworks with A = Sr, Ba. In this context the stability of $Sr_8Ga_{16}Ge_{30}$ is rationalized by longer Ga−Ge bonds preventing a distortion in the structure, while in the case of the missing "$Sr_8Al_{16}Si_{30}$" phase, the shorter polar covalent Al−Si bonds may cause the structure to distort. Theoretical calculations point to a very small band gap for the idealized ordered structure $Ba_8Al_6Si_{40}$ that closes upon addition of Al. It is also possible that the competing phase, $SrAl_2Si_2$, with its ordered Si−Al bonds, is more stable. Therefore a synthetic route that avoids this phase may be necessary to form the "$Sr_8Al_{16}Si_{30}$" phase. These observations lead to the suggestion that the composition "$Sr_8Al_{16}Si_{30}$" might be accessible via high-pressure synthesis.

ASSOCIATED CONTENT

Supporting Information

X-ray crystallographic data in CIF format for the single-crystal refinements of $Sr_8Al_{10}Si_{36}$ and $Ba_8Al_{10}Si_{36}$. The electrical transport, Rietveld refinement, and microprobe results are provided as a pdf (6 Pages). This material is available free of charge via the Internet at http://pubs.acs.org.

AUTHOR INFORMATION

Corresponding Author

*E-mail: smkauzlarich@ucdavis.edu.

Notes

The authors declare no competing financial interest.

ACKNOWLEDGMENTS

The authors would like to thank Michael Baitinger and Bodo Böhme for their assistance with the initial stages of this investigation and for insightful discussion; Greg Baxter, Brian Joy, and Sarah Roeske for sample polishing and assistance with microprobe analysis; Peter Klavins for assistance with electrical transport measurements. J.H.R. acknowledges an ICMR international research fellowship for travel funding to MPI Dresden. A.H. acknowledges support from the American Chemical Society, project SEED. This work was funded by NSF Grant DMR0600742, DMR1100313.

REFERENCES

(1) Kovnir, K. A.; Shevelkov, A. V. *Russ. Chem. Rev.* **2004**, *73*, 923−938.
(2) Christensen, M.; Johnsen, S.; Iversen, B. B. *Dalton Trans.* **2010**, *39*, 978−992.
(3) Chakoumakos, B. C.; Rawn, C. J.; Rondinone, A. J.; Stern, L. A.; Circone, S.; Kirby, S. H.; Ishii, Y.; Jones, C. Y.; Toby, B. H. *Can. J. Phys.* **2003**, *81*, 183−189.
(4) Eisenmann, B.; Schafer, H.; Zagler, R. *J. Less-Common Met.* **1986**, *118*, 43−55.
(5) Cordier, G.; Woll, P. *J. Less-Common Met.* **1991**, *169*, 291−302.
(6) Toberer, E. S.; Christensen, M.; Iversen, B. B.; Snyder, G. J. *Phys. Rev. B* **2008**, *77*, 075203.
(7) Saramat, A.; Svensson, G.; Palmqvist, A. E. C.; Stiewe, C.; Mueller, E.; Platzek, D.; Williams, S. G. K.; Rowe, D. M.; Bryan, J. D.; Stucky, G. D. *J. Appl. Phys.* **2006**, *99*, 023708.
(8) Chakoumakos, B. C.; Sales, B. C.; Mandrus, D. G.; Nolas, G. S. *J. Alloys Compd.* **2000**, *296*, 80−86.
(9) Sales, B. C.; Chakoumakos, B. C.; Jin, R.; Thompson, J. R.; Mandrus, D. *Phys. Rev. B* **2001**, *63*, 245113.
(10) Pacheco, V.; Bentien, A.; Carrillo-Cabrera, W.; Paschen, S.; Steglich, F.; Grin, Y. *Phys. Rev. B* **2005**, *71*, 165205.

(11) Bentien, A.; Pacheco, V.; Paschen, S.; Grin, Y.; Steglich, F. *Phys. Rev. B* **2005**, *71*, 165206.
(12) Yamanaka, S.; Enishi, E.; Fukuoka, H.; Yasukawa, M. *Inorg. Chem.* **1999**, *39*, 56−58.
(13) Liang, Y.; Böhme, B.; Reibold, M.; Schnelle, W.; Schwarz, U.; Baitinger, M.; Lichte, H.; Grin, Y. *Inorg. Chem.* **2011**, *50*, 4523−4528.
(14) Fukuoka, H.; Kiyoto, J.; Yamanaka, S. *Inorg. Chem.* **2003**, *42*, 2933−2937.
(15) Kawaji, H.; Horie, H.; Yamanaka, S.; Ishikawa, M. *Phys. Rev. Lett.* **1995**, *74*, 1427−1429.
(16) Neiner, D.; Okamoto, N. L.; Yu, P.; Leonard, S.; Condron, C. L.; Toney, M. F.; Ramasse, Q. M.; Browning, N. D.; Kauzlarich, S. M. *Inorg. Chem.* **2010**, *49*, 815−822.
(17) Kasper, J. S.; Hagenmul., P.; Pouchard, M.; Cros, C. *Science* **1965**, *150*, 1713−1714.
(18) Cros, C.; Pouchard, M.; Hagenmuller, P. *J. Solid State Chem.* **1970**, *2*, 570−581.
(19) Zaikina, J. V.; Kovnir, K. A.; Burkhardt, U.; Schnelle, W.; Haarmann, F.; Schwarz, U.; Grin, Y.; Shevelkov, A. V. *Inorg. Chem.* **2009**, *48*, 3720−3730.
(20) Condron, C. L.; Kauzlarich, S. M. *Inorg. Chem.* **2007**, *46*, 2556−2562.
(21) Condron, C. L.; Martin, J.; Nolas, G. S.; Piccoli, P. M. B.; Schultz, A. J.; Kauzlarich, S. M. *Inorg. Chem.* **2006**, *45*, 9381−9386.
(22) Tsujii, N.; Roudebush, J. H.; Zevalkink, A.; Cox-Uvarov, C. A.; Jeffery Snyder, G.; Kauzlarich, S. M. *J. Solid State Chem.* **2011**, *184*, 1293−1303.
(23) Roudebush, J. H.; Toberer, E. S.; Hope, H.; Snyder, G. J.; Kauzlarich, S. M. *J. Solid State Chem.* **2011**, *184*, 1176−1185.
(24) Rodriguez Carvajal, J. *Phys. B (Amsterdam, Neth.)* **1993**, *192*, 55−69.
(25) Sheldrick, G. M. *SADABS*; University of Göttingen: Göttingen, Germany, 1999.
(26) Sheldrick, G. M. *XRD Single-Crystal Software*; Bruker AXS: Madison, WI, 1999.
(27) Jepsen, O.; Burkhardt, A.; Andersen, O. K. *The Program TB-LMTO-ASA*, 4.7; Max-Planck-Institut für Festkörperforschung: Stuttgart, Germany, 1999.
(28) von Barth, U.; Hedin, L. *J. Phys. C* **1972**, *5*, 1629−1642.
(29) Andersen, O. K. *Phy. Rev. B: Condens. Matter Mater. Phys.* **1975**, *12*, 3060−3083.
(30) Kohout, M. *Int. J. Quantum Chem.* **2004**, *97*, 651−658.
(31) Kohout, M.; Wagner, F. R.; Grin, Y. *Int. J. Quantum Chem.* **2006**, *106*, 1499−1507.
(32) Kohout, M. *Faraday Discuss.* **2007**, 43−54.
(33) Bader, R. F. W. *Atoms in Molecules, A Quantum Theory*; Clarendon Press and Oxford University Press Inc: New York, 1994.
(34) Kohout, M. *Basin*, 4.4; 2008. For the further development of this software see http://www.cpfs.mpg.de/~kohout/dgrid.html.
(35) Eisenmann, B.; Schäfer, H.; Zagler, R. *J. Less-Common Met.* **1986**, *118*, 43−55.
(36) Kauzlarich, S. M.; Condron, C. L.; Wassei, J. K.; Ikeda, T.; Snyder, G. J. *J. Solid State Chem.* **2009**, *182*, 240−245.
(37) Nataraj, D.; Nagao, J. *J. Solid State Chem.* **2004**, *177*, 1905−1911.
(38) Beekman, M.; Nolas, G. S. *Int. J. Appl. Ceram. Technol.* **2007**, *4*, 332−338.
(39) Carrillo-Cabrera, W.; Budnyk, S.; Prots, I.; Grin, Y. *Z. Anorg. Allg. Chem.* **2004**, *630*, 2267−2276.
(40) Nataraj, D.; Nagao, J.; Ferhat, M.; Ebinuma, T. *J. Appl. Phys.* **2003**, *93*, 2424−2428.
(41) Toulemonde, P.; Adessi, C.; Blase, X.; San Miguel, A.; Tholence, J. L. *Phys. Rev. B* **2005**, *71*, 094504.
(42) Kozina, M.; Bridges, F.; Jiang, Y.; Avila, M. A.; Suekuni, K.; Takabatake, T. *Phys. Rev. B* **2009**, *80*, 212101.
(43) Jung, W.; Loerincz, J.; Ramlau, R.; Borrmann, H.; Prots, Y.; Haarmann, F.; Schnelle, W.; Burkhardt, U.; Baitinger, M.; Grin, Y. *Angew. Chem., Int. Ed.* **2007**, *46*, 6725−6728.
(44) Christensen, M.; Iversen, B. B. *Chem. Mater.* **2007**, *19*, 4896−4905.
(45) Paschen, S.; Carrillo-Cabrera, W.; Bentien, A.; Tran, V. H.; Baenitz, M.; Grin, Y.; Steglich, F. *Phys. Rev. B* **2001**, *64*, 214404.
(46) Uemura, T.; Akai, K.; Koga, K.; Tanaka, T.; Kurisu, H.; Yamamoto, S.; Kishimoto, K.; Koyanagi, T.; Matsuura, M. *J. Appl. Phys.* **2008**, *104*, 013702.
(47) Imai, M.; Kikegawa, T. *Inorg. Chem.* **2008**, *47*, 8881−8883.
(48) Imai, Y.; Watanabe, A. *Intermetallics* **2010**, *18*, 542−547.
(49) Wagner, F. R.; Bezugly, V.; Kohout, M.; Grin, Y. *Chem.—Eur. J.* **2007**, *13*, 5724−5741.
(50) Zhang, H.; Borrmann, H.; Oeschler, N.; Candolfi, C.; Schnelle, W.; Schmidt, M.; Burkhardt, U.; Baitinger, M.; Zhao, J. T.; Grin, Y. *Inorg. Chem.* **2011**, *50*, 1250−1257.